The coherent Hall effect of charge carriers in a superlattice: semiclassical description of the wavepacket dynamics

A B Hummel, T Bauer, E Mohler and H G Roskos

Physikalisches Institut der Johann Wolfgang Goethe–Universität, Max-von-Laue-Straße 1,
D-60438 Frankfurt am Main, Germany

Abstract
The coherent Hall effect of charge carriers is the quantum mechanical analogue
of the classical Hall effect for the case where the charge carriers are a coherent
ensemble of wavepackets. Kosevich considered this effect for the first time
for semiconductor superlattices subjected both to an electric field along the
growth direction and to a perpendicular magnetic field (Kosevich Y A 1999
Ann. Phys. **8** SI-145; 2001 *Phys. Rev.* B **63** 205313). The dynamics of the
charge carriers can be described successfully by means of a semiclassical
model mapping the equation of motion to a simple pendulum equation with
the deflection angle in the case of the pendulum being replaced by the k-
vector of the wavepackets along the superlattice's growth direction. While
Kosevich has presented an analytical treatment of the equation of motion, we
numerically solve it and compute the real-space and k-space trajectories of the
charge carriers. We thus arrive at a more illustrative and detailed analysis
of the wavepacket dynamics and make predictions for optical pump–probe
experiments which detect either the terahertz radiation emitted by the oscillating
charge carriers or the internal electric field as a function of time after impulsive
excitation of charge carriers.

1. Introduction

Since the early 1990s, the investigation of coherent phenomena of charge carriers in artificial
semiconductor structures, such as quantum wells and superlattices, ranks with the most
exciting topics in solid-state physics. Among these manifestations of the wave nature of the
charge carriers are Bloch oscillations (BOs), spatiotemporal oscillations expected to occur
in any periodic potential (as that of any crystal) under the influence of a static electric bias
field [1–4]. It took more than half a century from the first prediction of their existence to their
first experimental observation in semiconductor superlattices, i.e., one-dimensional artificial
lattices, by means of time-resolved laser spectroscopy [4–14].

In a semiclassical treatment, the angular BO frequency is proportional to both the spatial period d of the lattice potential and the electric field E:

$$\omega_{\mathrm{B}} = \frac{eEd}{\hbar}. \tag{1}$$

Typical superlattice periods are on the order of tens to hundreds of Å, i.e., by a factor of 10–100 larger than lattice periods of bulk semiconductors, resulting in BO frequencies in the THz regime, higher than the charge carriers' scattering rates at low temperatures. For bulk materials, the search for BOs has been unsuccessful until now. The high bias fields needed here either lead to competition with other phenomena such as Zener tunnelling [4] or to destruction of the material.

The appearance of an oscillatory electric current in a constant electric field contradicts Ohm's law, which predicts a stationary current. However, Ohm's law is an approximative description of carrier dynamics only valid in the classical limit. It does not hold immediately after the impulsive optical excitation of coherent wavepackets of charge carriers. It takes several scattering events to destroy their phase coherence and to enter the validity regime of Ohm's law. For superlattices excited close to the band-edge and at temperatures of several kelvin, this timescale is on the order of one to several picoseconds. During the dephasing time (also called coherence time here), one is able to investigate the manifestations of the coherent nature of the charge-carrier wavepackets. In this sense, BOs can be understood as the coherent analogue of transport according to Ohm's law.

Based on this knowledge, we intend to investigate the coherent analogue of the classical Hall effect as another, more complex solid-state phenomenon, arising upon transport of coherent charge-carrier wavepackets under the influence of a static magnetic field. While the classical Hall effect, as a manifestation of the particle nature of the charge carriers, is characterized by the build-up of a dc voltage (the Hall voltage), the coherent Hall effect of wavepackets is an ac-current phenomenon. One has to note that, despite the similarity in names, the effect is not directly related to the famous integer and fractional quantum Hall effects [15, 16]. While the latter are stationary manifestations of the wave nature of the charge carriers predominantly investigated in two-dimensional electron gases at low temperature, the former is a transient effect only arising upon superposition of wavefunctions and formation of wavepackets also in three-dimensional quantum systems in a Hall-type field situation.

We concentrate now on the investigation of the coherent Hall effect in superlattices, thus extending the research on BOs in superlattices to the case where an additional magnetic field is applied to the structure perpendicular to the electric field. The first theoretical study of such a system was performed by Kosevich based on an analytical treatment of the semiclassical equation of motion [17, 18]. Kosevich showed that the equation can be mapped to a simple pendulum equation. He predicted that its two fundamental solutions, corresponding to the oscillating and the rotating pendulum, respectively, have their analogues in two clearly separated regimes of motion of the charge carriers in the superlattice. While both regimes exhibit an oscillatory current along the direction of the classical Hall current, the dependence of the frequency on the applied electric and magnetic fields is very different.

Subsequent to Kosevich's predictions, we observed the ac current experimentally during the coherence time of impulsively excited carriers by applying a contactless measurement technique, time-resolved terahertz-emission spectroscopy [19, 20]. Additional information was obtained later with the help of time-resolved internal-electro-optic-sampling spectroscopy [21].

Recently, in light of fascinating dc current–voltage investigations of electron transport in non-perpendicular electric and magnetic fields aiming at evidence for chaotic carrier motion [22–24], we have extended our time-resolved studies, both theoretical and
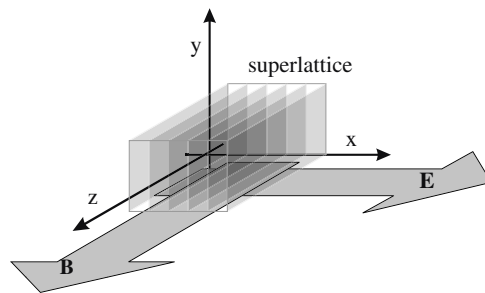
Figure 1. Scheme of the field geometry showing the directions of the electric field **E** and the magnetic field **B** in the superlattice. **E** is oriented along the superlattice growth direction while **B** is parallel to the superlattice layers.

experimental [25, 26], to arbitrary angles between the electric and magnetic fields. We have found evidence for a coherent coupling between Bloch and in-plane cyclotron oscillations in analogy to the Fiske effect of superconductor Josephson junctions coupled to an electromagnetic resonator. This work is, however, not the subject of the present publication.

The paper is organized as follows. In section 2, we outline the semiclassical single-particle model and put forth the analogy between the wavepacket dynamics and the motion of the classical pendulum to explain the existence of the two regimes of motion and to discuss in detail the expected dependence of the oscillation frequency on the electric and magnetic field strengths. Section 3 then deals with numerical results obtained for the parameters of a GaAs/AlGaAs superlattice structure employed in our past and ongoing experimental studies (1.7 nm thick $Al_{0.3}Ga_{0.7}As$ barriers and 9.7 nm thick GaAs wells). We present the trajectories of the charge carriers in real space and k-space, emphasizing the nonlinear character of the wavepacket motion in the spatial amplitude and the frequency spectrum of the oscillations in the two regimes of motion. We calculate the expected signals for two kinds of measurement techniques, THz-emission and internal electro-optic sampling spectroscopy.

2. Semiclassical model

2.1. Equation of motion

In this section, we set forth the equation of motion of a charged particle in a superlattice within the semiclassical single-band picture, following the treatment of [17, 18]. The semiclassical approach, where the wave nature of the charge carriers enters only via the superlattice band structure, has been found to be very successful in capturing the dominant features of the coherent-transport phenomena considered here [19].

The charge carrier is under the influence of both an electric field **E**, which is oriented along the superlattice growth direction denoted as the x-direction, and a magnetic field **B**, which is parallel to the semiconductor layers and whose direction defines the orientation of the z-axis (see figure 1). The build-up of a Hall electric field is considered negligible, (i) because we investigate only the first few picoseconds after impulsive excitation of the charge carriers at a low density, and (ii) because of screening by the contacts which sandwich the superlattice. If not mentioned otherwise, we will neglect dephasing, which mainly leads to an exponential damping of the coherent signals.

We furthermore consider only the single-particle effects. Basic Coulomb corrections for moderate carrier density have been addressed by Kosevich [17, 18]. They modify the findings

to be presented in the following by shifting the characteristic oscillation frequencies. It turns out that, for sufficiently low carrier density (see below), all results obtained by the single-particle model remain valid if the cyclotron frequency ω_C (see equation (12)) is replaced by the frequency Ω given by $\Omega^2 = \omega_C{}^2 + \omega_{P\parallel}{}^2 + \omega_0^2$. Here, $\omega_{P\parallel} = \sqrt{nq^2/m_x\epsilon\epsilon_0}$ is the frequency of the collective magneto-plasma oscillations of the charge carriers along the growth axis of the superlattice. The ω_0^2-term accounts for a blue-shift of Ω^2 resulting from the effective electron–hole potential. The shift amounts to $\omega_0^2 = \gamma q^2/m_x a_B^3 \epsilon\epsilon_0$, with $a_B = \hbar^2 4\pi\epsilon\epsilon_0/m^* q^2$ being Bohr's radius. The dimensionless parameter γ is related to the exciton binding energy and could be determined experimentally to be $\gamma \approx 0.1/4\pi \approx 8 \times 10^{-3}$ [27]. Note that the corrections are only meaningful if $\omega_{P\parallel}$, $\omega_0 < \omega_C$, respectively $\omega_{P\parallel}$, $\omega_0 < \omega_B$, otherwise the two regimes of motion do not exist. For their observation, experiments hence have to be performed at sufficiently low carrier densities.

On this basis, the dynamics of the wavepackets is determined by the Lorentz force $\mathbf{F}_L$

$$\hbar \dot{\mathbf{k}} = \mathbf{F}_L = q \, (\mathbf{E} + \mathbf{v} \times \mathbf{B}) \tag{2}$$

and the general dispersion relation

$$\mathbf{v} = \frac{1}{\hbar} \frac{\partial \varepsilon(\mathbf{k})}{\partial \mathbf{k}}. \tag{3}$$

$\hbar$, q, and $\mathbf{k}$ denote Planck's constant divided by 2π, the charge carrier's electric charge, and its wavevector, respectively. The group velocity $\mathbf{v}$ is proportional to the first $\mathbf{k}$ derivative of the miniband energy $\varepsilon(\mathbf{k})$. In the framework of a tight-binding calculation, $\varepsilon(\mathbf{k})$ is cosine shaped along the superlattice growth direction [29, 30]. Parallel to the semiconductor layers, $\varepsilon(\mathbf{k})$ has the typical paraboloidal shape of the bulk semiconductor material characterized by its constant effective mass m^*:

$$\varepsilon(\mathbf{k}) = \frac{\Delta}{2} [1 - \cos(k_x d)] + \frac{\hbar^2}{2m^*} \left(k_y^2 + k_z^2 \right). \tag{4}$$

Δ denotes the width of the miniband of the superlattice, d the spatial period. Due to (3) and (4), the velocity components are given by

$$v_x = \frac{\Delta d}{2\hbar} \sin(k_x d), \qquad v_{y,z} = \frac{\hbar}{m^*} k_{y,z}. \tag{5}$$

The evaluation of the vector product in equation (2) is simplified by the chosen field geometry. $\dot{\mathbf{k}}$ evaluates to

$$\dot{\mathbf{k}} = (\dot{k}_x, \, \dot{k}_y, \, \dot{k}_z) = \frac{q}{\hbar} \left(E + v_y B, \, -v_x B, \, 0 \right). \tag{6}$$

The solution of k_z is a constant $k_z(t) = k_z(0)$, which will be omitted from now on. Using equation (5), the velocities v_x and v_y in equation (6) can be eliminated, resulting in two coupled differential equations

$$\dot{\mathbf{k}} = (\dot{k}_x, \, \dot{k}_y) = \frac{q}{\hbar} \left(E + \frac{\hbar}{m^*} B k_y, \, -\frac{\Delta d}{2\hbar} B \sin(k_x d) \right). \tag{7}$$

With the miniband dispersion being cosine shaped, the miniband width Δ and the effective mass m_x at the bottom of the miniband are related to each other:

$$\frac{\Delta d}{2\hbar^2} = \frac{1}{m_x d}. \tag{8}$$

Using equation (8) and applying the transformation

$$k_i \to \tilde{k}_i = k_i d \qquad i = x, y, \tag{9}$$

equation (7) becomes a system of differential equations for the dimensionless wavevector $\tilde{\mathbf{k}}$

$$\left(\dot{\tilde{k}}_x, \dot{\tilde{k}}_y\right) = \left(\omega_B + \omega_C^* \tilde{k}_y, -\omega_C^x \sin\left(\tilde{k}_x\right)\right), \tag{10}$$

where $\omega_B = qEd/\hbar$ is the BO frequency as in the absence of a magnetic field, and $\omega_C^* = qB/m^*$ and $\omega_C^x = qB/m_x$ denote the bulk GaAs cyclotron frequency and the cyclotron frequency of a charge carrier with a constant bottom-miniband mass m_x, respectively.

The first-order coupled differential equations (10) can be condensed into a second-order differential equation

$$\ddot{\tilde{k}}_x = -\omega_C^* \omega_C^x \sin(\tilde{k}_x) = -\omega_C^2 \sin(\tilde{k}_x), \tag{11}$$

where

$$\omega_C = \frac{qB}{\sqrt{m^* m_x}}. \tag{12}$$

Equation (11) is the pendulum equation with the dimensionless wavevector $\tilde{k}_x$ playing the part of the pendulum's deflection angle φ. ω_C is the eigenfrequency for small amplitudes of $\tilde{k}_x$. Due to this analogy it is quite helpful to analyse the wavepacket dynamics using equation (11) since it elucidates in a very clear manner the influence of the two parameters E and B on the character of the motion.

The time-independent solutions $\tilde{\mathbf{k}}(t) = \tilde{\mathbf{k}}^{\text{stat}} = \text{const}$ of equation (10) resulting from

$$\mathbf{0} = \left(\omega_B + \omega_C^* \tilde{k}_y^{\text{stat}}, -\omega_C^x \sin\left(\tilde{k}_x^{\text{stat}}\right)\right) \tag{13}$$

are

$$\left(\tilde{k}_x^{\text{stat}}, \tilde{k}_y^{\text{stat}}\right) = \left(n\pi, -\frac{\omega_B}{\omega_C^*}\right) \qquad n = 0, \pm 1, \pm 2, \ldots. \tag{14}$$

If one restricts the discussion to the first mini-Brillouin zone with $|\tilde{k}_x| \leqslant \pi$, only $n = 0$ and the two equivalent solutions $n = \pm 1$ are to be considered. The two solutions correspond to the upper unstable and the lower stable fixed point of the pendulum at $\varphi = \pm\pi$ and 0, respectively. It can be seen from equation (5) that in both cases the group velocity along the superlattice growth direction vanishes. In the y-direction, perpendicular to $\mathbf{E}$ and $\mathbf{B}$, the charge carrier has a constant drift velocity $v_y^{\text{stat}} = \hbar \tilde{k}_y^{\text{stat}}/m^* d = -E/B$, which is determined only by the ratio of E and B. At this point, the sum of all forces originating from external fields vanishes ($\hbar \dot{\mathbf{k}}^{\text{stat}} = \mathbf{F}_L = \mathbf{0}$). The magnetic component of the Lorentz force $q \mathbf{v} \times \mathbf{B}$ is exactly compensated by the Coulomb force $q \mathbf{E}$ on the charge carrier.

2.2. The two regimes of motion

Depending on the ratio E/B, the charge carrier is in either one of two clearly separated regimes of motion. Figure 2 illustrates this for $\mathbf{k}$-space.

Projection onto the $\tilde{k}_x$-axis shows one regime which corresponds to the oscillating pendulum (lower part of figure 2), and another one which is analogous to the rotating pendulum (upper part of figure 2).

In the first case, the magnetic field is strong enough to confine the motion of the charge carrier to the first mini-Brillouin zone $-\pi < \tilde{k}_x < \pi$, and the carrier oscillates around $\tilde{k}_x = 0$. This regime has been termed the *bottom-miniband* regime in [18], or the *cyclotron-like* regime because of the analogy to carrier motion in bulk semiconductors under the influence of a strong magnetic field.

In the other case, for dominating electric field, $\tilde{k}_x$ periodically crosses the mini-Brillouin zone boundaries. The charge carrier moves along the whole cosine-shaped dispersion curve
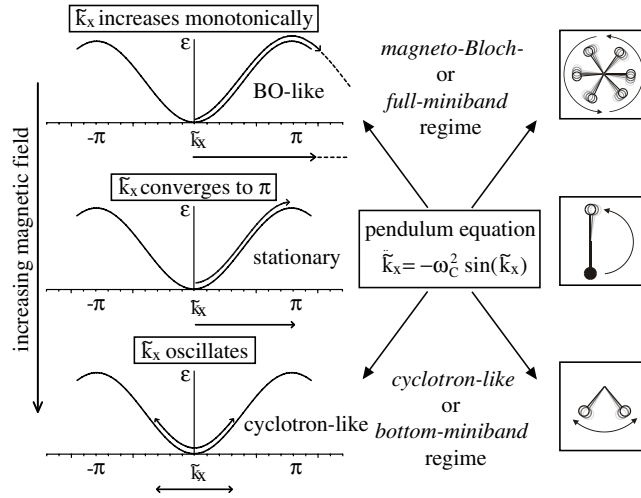
Figure 2. A charge carrier in a semiconductor superlattice under the simultaneous influence of a magnetic and an electric field may be viewed in analogy to a rigid mechanical pendulum (right side). Depending on the ratio E/B, different types of motion may be observed for propagation along $\tilde{k}_x$ (left side).

since $\tilde{k}_x$ continuously increases (or decreases, depending on the sign of **E**). The resulting carrier dynamics is very similar to that of pure BOs where $\tilde{k}_x$ increases linearly in time. Hence, this regime has been named the *magneto-Bloch* or *full-miniband* regime.

The transition point, corresponding to the pendulum remaining at the upper fixed point, is reached when the charge carrier remains located at $\tilde{k}_x = \pm\pi$ (middle part of figure 2).

Although both types of motion lead to an oscillatory carrier dynamics in real space, the dependence of the frequency on the external fields is different in the two regimes. Again, this can be understood by recalling that $\tilde{k}_x$ obeys the non-linear pendulum equation (11). While $\tilde{k}_x$ corresponds to the angle φ, ω_C plays the part of the pendulum's eigenfrequency $\omega = \sqrt{g/l} = 2\pi/T$, where g is the gravitational acceleration, l denotes the length of the pendulum, and T is the oscillation period. T and thus ω depend on the initial deflection angle φ_0 and the initial angular velocity $\dot{\varphi}_0$ at time $t = 0$, or equivalently, on the constant total mechanical energy (sum of the kinetic and the potential energies) $W^{\text{tot}} = m(\dot{\varphi}_0 l)^2/2 + mgl(1 - \cos\varphi_0)$ of the pendulum. Here, m denotes the pendulum's mass.

In the case of an oscillating pendulum, T increases when W^{tot} is raised. This well known result is a consequence of the fact that the back-driving force rises sublinearly with the pendulum's deflection φ. At a certain total energy $W^{\text{trans}} = 2\,mgl$, the pendulum will reach its upper turning point ($\varphi = \pm\pi$) and remain there. Hence, T diverges when W^{tot} approaches W^{trans}. Any slight increase of W^{tot} will lead to a transition to rotation. With rising W^{tot}, T then decreases, since the amount of kinetic energy that can be converted to potential energy is limited at fixed pendulum length l.

For $W^{\text{tot}} = W^{\text{trans}}$, the initial angular velocity $\dot{\varphi}_0^{\text{trans}}$ at which the transition between the two regimes occurs evaluates to $\dot{\varphi}_0^{\text{trans}} = \omega\sqrt{2(1 + \cos\varphi_0)}$. For the special case of $\varphi_0 = 0$ this further reduces to $\dot{\varphi}_0^{\text{trans}} = 2\,\omega$. In analogy, the condition of transition for a wavepacket in a semiconductor superlattice can be written as

$$\dot{\tilde{k}}_{x,0}^{\text{trans}} = \omega_C\sqrt{2\left(1 + \cos(\tilde{k}_{x,0})\right)} \qquad (15)$$

and

$$\dot{\tilde{k}}_{x,0}^{\text{trans}} = 2\,\omega_{\text{C}} \qquad \text{for } \tilde{k}_{x,0} = 0. \tag{16}$$

The special case of $\tilde{k}_{x,0} = 0$ is interesting since it can be prepared easily in the experiment via excitation of the superlattice at the miniband edge. Then, $\tilde{k}_{x,0} = \tilde{k}_{y,0} = 0$. Applying these initial conditions to equation (10) results in

$$\begin{aligned}
\dot{\tilde{k}}_{x,0} &= \omega_{\text{B}} = \frac{q\,E\,d}{\hbar} \\
\dot{\tilde{k}}_{y,0} &= 0,
\end{aligned} \tag{17}$$

which describe the motion of a charge carrier which initially is at rest, but is then accelerated by the Coulomb force acting in the x-direction.

Obviously, the Bloch frequency ω_{B}, with its magnitude determined by the absolute value of the electric field $\mathbf{E}$, corresponds to the initial angular velocity $\dot{\varphi}_0$ in the pendulum picture. On the other hand, the cyclotron frequency ω_{C}, determined by the absolute value of the magnetic field $\mathbf{B}$, acts as the back-driving force in the mechanical model. The stronger the back-driving force, the higher the initial angular velocity needed in order to reach the transition point. Hence, the transition between the magneto-Bloch regime and the cyclotron-like regime will depend on the ratio of E and B.

The qualitative frequency dependence on the external fields E and B can be predicted using the pendulum picture as follows. For a given electric field and absent magnetic field, the wavepacket performs the well known BOs, characterized by a linear increase of $\tilde{k}_x$. The resulting oscillatory motion in real space originates from the dispersion relation of the superlattice (see equations (4) and (5)). The case of $\tilde{k}_x$ increasing linearly in time corresponds to a pendulum performing an unperturbed rotation without any gravitational influence ($g = 0$), where $\varphi(t)$ increases linearly. The total energy of the pendulum is simply its kinetic energy which is determined by the initial angular velocity $\dot{\varphi}_0$ (electric field in the case of the charge carrier). An increasing back-driving force corresponding to an increasing magnetic field will slow down the rotation, resulting in a decrease of frequency. At a certain value of the back-driving force (magnetic field), the pendulum (the charge carrier) will converge to the time-independent solution at $\varphi = \pi$, $\dot{\varphi} = 0$ ($\tilde{k}_x = \pi$, $\dot{\tilde{k}}_x = 0$) where the oscillation period T diverges, i.e., the frequency drops down to zero. A further increase of gravitational acceleration (magnetic field) will then lead to an oscillatory type of motion with increasing frequency for increasing g (B).

For a constant gravitational acceleration g (magnetic field B), the frequency's dependence on the initial angular velocity (electric field) is opposite. The frequency of the rotating pendulum (Bloch-like motion) increases with rising initial angular velocity $\dot{\varphi}_0$ (E), i.e., for increasing energy. In contrast, the frequency of the oscillating pendulum (cyclotron-like motion) will decrease with increasing $\dot{\varphi}_0$ (E), since the maximal oscillation amplitude rises and hence, as noted before, so does the oscillation period.

As can be seen from equations (16) and (17), the transition between the two regimes of frequency behaviour occurs at

$$\omega_{\text{B}} = 2\,\omega_{\text{C}} \tag{18}$$

for a charge-carrier wavepacket created at the bottom of the miniband ($\tilde{k}_{x,0} = \tilde{k}_{y,0} = 0$). The motion converges to the non-oscillatory solution with a vanishing velocity component v_x along the growth axis and a constant drift velocity $v_y = -E/B$ in the y-direction (equations (5) and (14)). In the case $\omega_{\text{B}} > 2\,\omega_{\text{C}}$, the charge carrier is in the magneto-Bloch or full-miniband regime and $\tilde{k}_x$ increases monotonically but not necessarily linearly with time—like the rotating

pendulum under the influence of gravitation, where the angular velocity $\dot{\varphi}$ varies between a maximum at $\varphi = 0$ and a minimum at $\varphi = \pm\pi$ without changing its sign. The direction of rotation is preserved. If $\omega_B < 2\omega_C$, the motion is cyclotron-like and more or less restricted to the bottom of the miniband where the value of $\tilde{k}_x$ oscillates between $\pm\kappa$ with $0 < \kappa < \pi$.

2.3. Analytical solutions for the oscillation frequency

2.3.1. Magneto-Bloch regime. More quantitative results for the oscillation period T, and hence the oscillation frequency, can be obtained by solving equation (11) analytically. For the mechanical pendulum, the total energy W^{tot} and hence $2\,W^{\text{tot}}/ml^2 = \dot{\varphi}^2 + 2\,\omega^2(1 - \cos\varphi) = \dot{\varphi}^2 + 4\,\omega^2\sin^2(\varphi/2)$ are constants. In analogy, the dimensionless wavevector obeys the relation

$$C = \dot{\tilde{k}}_x^2 + 4\omega_C^2\,\sin^2\left(\tilde{k}_x/2\right). \tag{19}$$

With equation (17), the constant C evaluates to $C = \dot{\tilde{k}}_{x,0}^2 = \omega_B^2$ for the special case of a wavepacket generated at the bottom of the miniband ($\tilde{k}_{x,0} = \tilde{k}_{y,0} = 0$). Solving equation (19) for the time t results in

$$t = 2 \int_0^{\tilde{k}_x/2} \sqrt{\frac{1}{\omega_B^2 - 4\omega_C^2\sin^2(\beta)}}\,\mathrm{d}\beta. \tag{20}$$

If the charge carrier performs a magneto-Bloch-type motion, and $\omega_B \gg \omega_C$ the integral in equation (20) can be solved approximately by expanding the square root up to the first order:

$$t \approx \frac{\tilde{k}_x(t)}{\omega_B} + \frac{J}{\omega_B} \int_0^{\tilde{k}_x/2} \sin^2(\beta)\,\mathrm{d}\beta, \tag{21}$$

where $J = (\frac{2\omega_C}{\omega_B})^2 \ll 1$. In general, $\int \sin^2(\beta)\,\mathrm{d}\beta = -\sin(2\beta)/4 + \beta/2 + \text{const}$, but since we are only interested in the harmonic part of the wavepacket's velocity at the moment, i.e., only want to investigate how the fundamental frequency evolves with increasing magnetic field, we determine the *average* slope of $\tilde{k}_x(t)$ by calculating $\tilde{k}_x(t)/t$ for $t \to \infty$. In this case, $\tilde{k}_x(t) \gg \sin(\tilde{k}_x(t))$, and the term $-\sin(\tilde{k}_x)/4$ can be neglected. We obtain

$$\tilde{k}_x(t) \approx \omega_B \left(\frac{\omega_B^2}{\omega_B^2 + \omega_C^2}\right) t = \omega_{\text{MB}}\,t. \tag{22}$$

Because of $\omega_C \ll \omega_B$, the magneto-Bloch frequency ω_{MB} introduced in equation (22) can be approximated by

$$\omega_{\text{MB}} \approx \omega_B - \frac{\omega_C^2}{\omega_B}. \tag{23}$$

The principal dependences of the oscillation frequency on the external fields are as expected from the qualitative discussion above. An increasing electric field (increasing ω_B) raises ω_{MB}; an increasing magnetic field (increasing ω_C) leads to a decrease of ω_{MB}. For larger ratios of ω_C and ω_B (larger J), the Taylor expansion of the square root in equation (20) must be extended beyond the first-order term. Neglecting the numerous trigonometric terms originating from the integration of $\sin^n(\beta)$ ($n = 2, 4, \ldots$), which again are not relevant for the fundamental frequency (they only cause $\tilde{k}_x(t)$ to additionally oscillate while growing monotonically), results
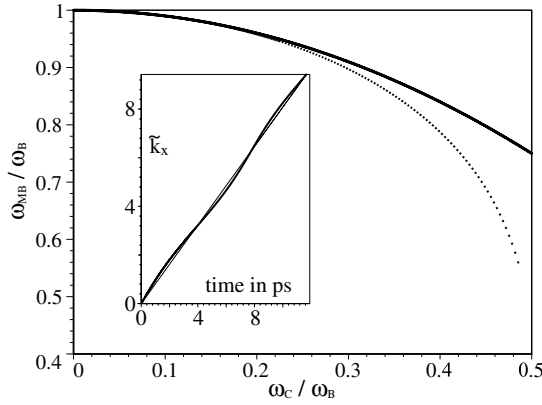
Figure 3. Bold line: first-order approximation of the magneto-Bloch frequency according to equation (23). Dotted line: magneto-Bloch frequency obtained by Taylor expansion up to 50th order. This solution is close to reality; a comparison with an expansion to 250th order (not shown) exhibits visible deviations only for values of $\omega_C/\omega_B > 0.48$. Inset: influence of the neglected trigonometric term in the solution of equation (21) on $\tilde{k}_x$. The straight line corresponds to the relation between time t and wavevector $\tilde{k}_x$ of equation (22) calculated with $\omega_C = 0.49\,\omega_B$ ($J = 0.95$) in order to enhance the effect (note that for this large value of J equation (21) is not a very good approximation any more).

in

$$t = \frac{2\tilde{k}_x}{\omega_B}\left(\frac{1}{2} + \frac{1}{8}\,J + \frac{9}{128}\,J^2 + \frac{25}{512}\,J^3 + \frac{1225}{32\,768}\,J^4 + \frac{3969}{131\,072}\,J^5 + \cdots\right) = \frac{2\tilde{k}_x}{\omega_B}\,f(J).$$

(24)

This relation can be used to derive $\omega_{MB} = \tilde{k}_x/t$ by expanding $1/f(J)$ around $\omega_C = 0$ to higher orders:

$$\omega_{MB} = \omega_B - \frac{\omega_C^2}{\omega_B} - \frac{5}{4}\frac{\omega_C^4}{\omega_B^3} - \frac{11}{4}\frac{\omega_C^6}{\omega_B^5} - \frac{469}{64}\frac{\omega_C^8}{\omega_B^7} - \cdots.$$

(25)

A comparison with equation (23) shows that the first two terms are identical. For higher magnetic fields, the frequency decreases faster than expected by the simple equation as illustrated in figure 3. Here, the first order approximation (equation (23)) and a solution originating from a Taylor expansion up to the 50th order are depicted. The decrease of the frequency toward zero for $\omega_B \rightarrow 2\omega_C$ (as expected from the pendulum picture) is clearly visible for the higher-order approximation (equation (25)). The inset of figure 3 depicts the influence of the neglected trigonometric term in the solution of equation (21) on $\tilde{k}_x(t)$. In the case of the expansion according to equation (24), the consideration of the respective trigonometric terms would lead to even stronger additional oscillations, but again these oscillations take place around a straight line with its slope corresponding to the fundamental frequency ω_{MB} of the system. This is fully analogous to the behaviour of the pendulum. For a very fast rotation of the pendulum (magneto-Bloch regime of the charge-carrier motion), the angle ($\tilde{k}_x$) increases almost linearly in time. When the pendulum slows down, its angular velocity becomes more and more influenced by the back-driving force (magnetic field). The pendulum will move faster around its rest position than around its upper point of return; the angular momentum and of course the angle itself are modulated periodically. The motion is not harmonic any more.

2.3.2. Cyclotron-like regime. In the case of large magnetic fields, one expects an oscillatory solution of the pendulum equation and small values of $\tilde{k}_x$. One therefore approximates $\sin(\beta)$ by β in equation (20), so that for the oscillation period and subsequently for $\tilde{k}_x$ there follows

$$t = \frac{1}{\omega_C} \arcsin\left(\tilde{k}_x(t) \frac{\omega_C}{\omega_B}\right) \implies k_x(t) = \frac{\omega_B}{\omega_C d} \sin(\omega_C t). \tag{26}$$

With equation (5) and the definitions of ω_C and ω_B (equations (1), (12)), and with equation (8), we obtain for the velocity along the growth axis

$$v_x = \frac{\Delta d}{2\hbar} \sin(k_x(t) d) \approx \frac{\Delta d}{2\hbar} k_x(t) d = \frac{E}{B} \sqrt{\frac{m^*}{m_x}} \sin(\omega_C t). \tag{27}$$

Hence, in the limit of a very large magnetic field, the charge-carrier wavepacket oscillates with the cyclotron frequency ω_C, which is a linear function of the magnetic field, and independent of the electric field.

3. Numerically calculated wavepacket trajectories

The numerical solution of the equation of motion permits us both to determine the exact temporal behaviour of the wavepacket oscillations across the whole range of electric and magnetic fields and to visualize the charge-carrier trajectories both in **k**-space and in real space. We numerically integrate the differential equation for the vector **u**

$$\mathbf{u} = (u_1, u_2, u_3, u_4)^T = (\tilde{k}_x, \tilde{k}_y, x, y)^T \tag{28}$$

for the initial condition $\mathbf{u}(0) = \mathbf{0}$. This condition corresponds to the excitation of a wavepacket at the bottom of the miniband, as done in the experiments. With the differential equation (10) for $\tilde{k}_x$ and $\tilde{k}_y$, and with equations (5) for the velocities v_x and v_y, the differential equation for **u** can be written as

$$\frac{\mathrm{d}}{\mathrm{d}t}\mathbf{u} = \begin{pmatrix} \omega_B + \omega_C^* u_2 \\ -\omega_C^x \sin(u_1) \\ \frac{\Delta d}{2\hbar} \sin(u_1) \\ \frac{\hbar}{m^* d} u_2 \end{pmatrix}. \tag{29}$$

The calculations are performed for $q = e$ (positive elementary charge), a miniband width $\Delta = 20$ meV, a superlattice period of $d = 11.4$ nm, and conduction-band mass parameters $m^* = 0.068\, m_0$ and $m_x = \frac{2\hbar^2}{\Delta d^2} = 0.058\, m_0$ (see equation (8)), with m_0 being the rest mass of an electron in vacuum.

3.1. Numerical calculations for **k**-space

We begin by studying the time dependence of the dimensionless wavevector $\tilde{k}_x$ in more detail.

Figure 4 shows $\tilde{k}_x$-transients in the magneto-Bloch regime for an electric field of 5 kV cm^{-1} and magnetic fields between 0 and 1.554 T. The transition to the cyclotron-like regime occurs at a magnetic field of about $B_T = 1.554\,48\dots$ T. At zero magnetic field (pure BOs), $\tilde{k}_x$ increases linearly in time and its slope corresponds to the BO frequency ω_B. With increasing magnetic field, the trajectories become periodically modulated while their overall slope sinks. The latter is related to the reduction of the fundamental frequency of the charge-carrier oscillations in real space, while the modulation of the k-space trajectories leads to overtones in the frequency spectrum. The plots of figure 4 underscore why this regime of motion has been termed the *magneto-Bloch* regime: despite the influence of the magnetic field, $\tilde{k}_x$ increases monotonically without any restrictions as for pure BOs.
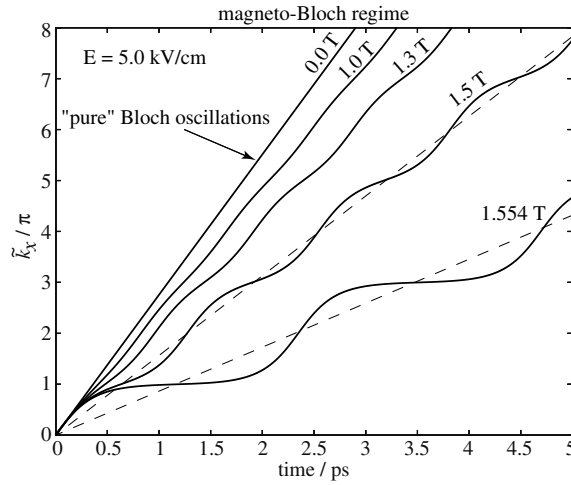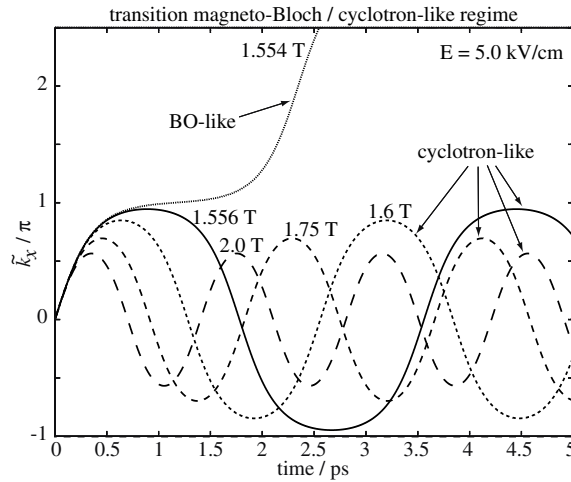
Figure 4. Temporal evolution of $\tilde{k}_x$ for a constant electric field of 5 kV cm^{-1} and various magnetic fields in the magneto-Bloch regime. The values ± 1 of the dimensionless quantity $\tilde{k}_x/\pi$ delimit the first Brillouin zone.

Figure 5. Temporal evolution of $\tilde{k}_x$ for a constant electric field of 5 kV cm^{-1} and various magnetic fields in the magneto-Bloch and the cyclotron-like regimes of motion.

The transition to the cyclotron-like regime of motion takes place when the modulation of $\tilde{k}_x$ by the magnetic field becomes so strong that $\tilde{k}_x$ runs parallel to the time axis at its flattest points ($\dot{\tilde{k}}_x = 0$). The transition is illustrated in figure 5. In the cyclotron-like regime, $\dot{\tilde{k}}_x$ changes sign time and again. The result is an oscillatory confinement of $\tilde{k}_x$ within the first mini-Brillouin zone. The oscillation frequency increases with B as known for cyclotron oscillations, which underscores the reason for the term *cyclotron-like*.

Figure 6 displays the motion of a wavepacket on the energy contour of the two-dimensional ($\tilde{k}_x, \tilde{k}_y$)-space for an electric field of 5 kV cm^{-1} and various magnetic fields. The figure once more illustrates the fundamental difference between the trajectories in the two regimes. In the magneto-Bloch regime (1.2 and 1.5 T), the wavepacket can overcome the boundary between
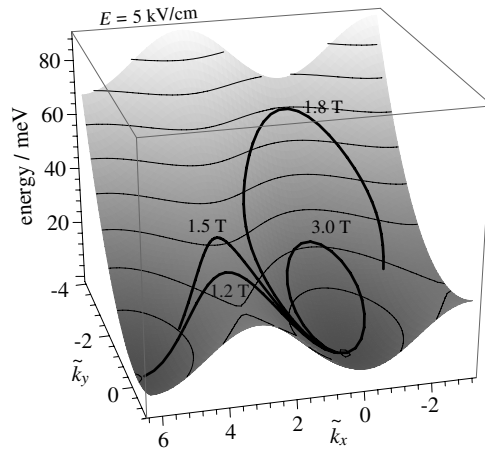
Figure 6. Charge-carrier trajectories on the energy-band contour (grey-shaded surface) of the superlattice for four different magnetic fields, but constant electric field (5 kV cm^{-1}). The trajectories are open in the magneto-Bloch regime (1.2 and 1.5 T), but form closed loops in the cyclotron-like regime of motion (1.8 and 3.0 T). The curve for 1.8 T is not completed for clarity.
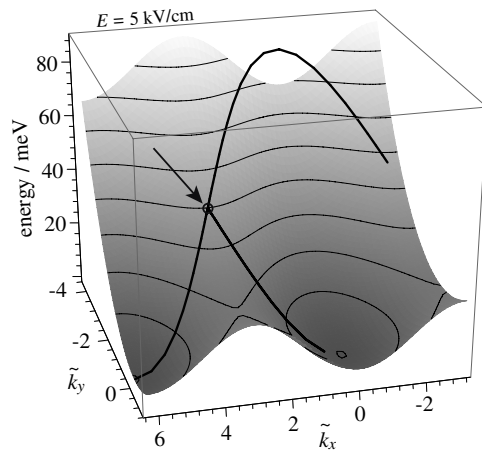

Figure 7. Two trajectories close to the transition between the regimes. The difference in magnetic field is only $\Delta B = 10^{-5}$ T.

the first and the second mini-Brillouin zone at $\tilde{k}_x = \pi$, and the result is an open curve in k-space. In the cyclotron-like regime (1.8 and 3 T), the curves are closed and lie within the first mini-Brillouin zone.

Figure 7 displays two trajectories just barely above and below the transition, with the difference in magnetic field being $\Delta B = 10^{-5}$ T. A trajectory directly at the transition would start at $\tilde{k}_x = 0$ and stop and remain at $\tilde{k}_x^{\text{stat}} = \pi$ (the stationary solution corresponding to a wavepacket drifting at a constant velocity in real space). Slightly off the transition point, the trajectories are nearly impossible to distinguish from this one, until very close to $\tilde{k}_x^{\text{stat}} = \pi$ (marked by an arrow) they branch off into different directions, in one case running in a closed loop, in the other case along an open path.
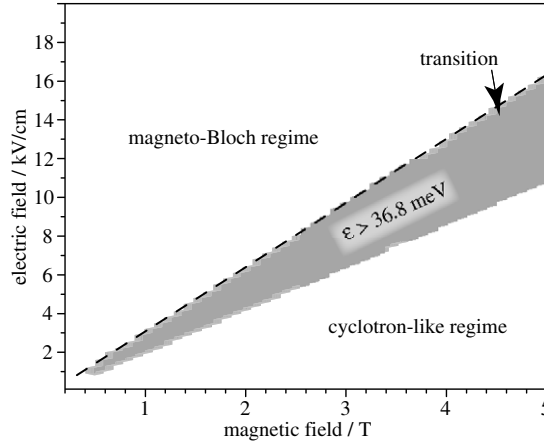
Figure 8. Regions in E–B parameter space where the charge carriers can undergo optical-phonon emission (area shaded in grey). The transition between the magneto-Bloch and the cyclotron-like regimes of motion is indicated by a dashed line. Optical-phonon emission is possible in the cyclotron-like regime in the vicinity of the transition.

We end this section by noting that a study of the trajectories in $(\tilde{k}_x, \tilde{k}_y)$-space (see the last two figures) can also help to identify optical-phonon scattering channels which contribute to energy loss and dephasing of the wavepackets. Although the miniband width of $\Delta = 20$ meV, assumed in our simulations, is smaller than the optical-phonon energy of $E_{\mathrm{ph}} = 36.8$ meV for GaAs, it would be incorrect to assume that scattering by emission of optical phonons is inactive [31, 32]. In particular, close to the transition between the two regimes of motion, the energy contribution of wavepacket motion along the y-direction can be substantial, raising the total kinetic energy of the wavepackets periodically to values well above E_{ph}.

For the superlattice parameters considered here, figure 8 shows the values of the electric and magnetic fields, for which the charge carriers can reach kinetic energies above E_{ph} and suffer energy and phase loss by optical-phonon emission. For our parameters, this is mainly the case in the cyclotron-like regime.

3.2. Numerical calculations for real space

We now come to a detailed investigation of real-space carrier motion.

Figure 9 shows calculated charge-carrier trajectories in real space for a constant electric field of 5 kV cm^{-1} and various magnetic fields. All trajectories are plotted for a time window of 5 ps after excitation of the carrier at $t = 0$ at the position $x = y = 0$ and with initial speed $\dot{x} = \dot{y} = 0$. The x-values are given in units of the superlattice period d.

The trajectories for 1.3 and 1.55 T are representative for the magneto-Bloch regime, those for 1.6 and for 2 T for the cyclotron-like regime of motion; 1.554 4819 . . . T corresponds to the magnetic field B_{T} at the transition between the two regimes. As mentioned before, in this case all oscillations disappear, as the charge carrier is accelerated to a constant drift velocity along the y-axis, i.e., along the direction perpendicular to both the electric and magnetic fields. The other trajectories exhibit an oscillatory cycloid-like shape. Concerning the oscillation frequency, we find confirmed what we have discussed before. For dominating electric field, in the magneto-Bloch regime, the frequency decreases with increasing magnetic field. On the other hand, in the cyclotron-like regime of motion, for dominating magnetic field, it increases as known from pure cyclotron oscillations.
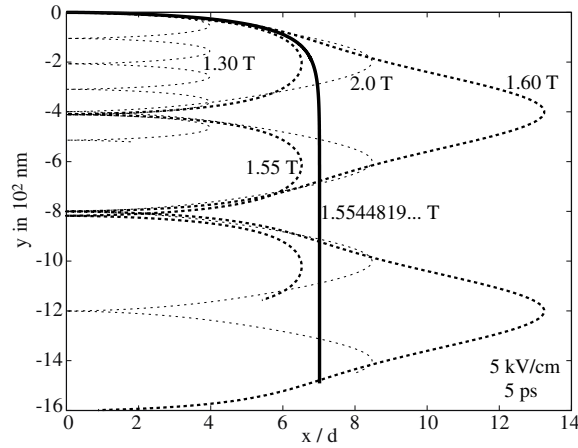
Figure 9. Wavepacket trajectories in real space for a constant electric field of 5 kV cm^{-1} and various magnetic fields as indicated in the figure. The charge carrier is initially ($t = 0$) at the upper left corner of the plot ($x = 0$, $y = 0$). Shown are the first 5 ps of the motion at the transition (bold type), in the magneto-Bloch (1.30 and 1.55 T) and in the cyclotron-like regimes of motion (1.60 and 2.0 T).

Although the trajectories in the two regimes may look similar at first glance, they exhibit one fundamental difference: a change in curvature at approximately half of the maximum amplitude only observed in the cyclotron-like regime. The curvature change can be seen nicely in the trajectory for 1.6 T. Recalling the oscillatory nature of wavepacket motion in k-space in this regime, this feature can be associated with the slowing down of the wavepacket and its stopping at the point of return in k-space before it is accelerated downwards again. In real space, the direction of motion does not change during the reversal of the propagation direction in k-space because the sign of $\frac{\partial \varepsilon(\mathbf{k})}{\partial \mathbf{k}}$ and hence the sign of the group velocity of the wavepacket (see equation (3)) do not change.

A striking feature of the real-space trajectories is the strong increase of the maximum displacement along the x-axis for rising magnetic field in the vicinity of the transition. The largest displacement is reached in the cyclotron-like regime. In the following, we investigate the field dependence of the x-displacement in more detail.

3.2.1. Maximum spatial x-displacement. An analytical determination of the maximum spatial displacement is possible based on the formal integration of the following expression for v_x obtained from equations (5) and (11):

$$v_x = -\frac{\Delta\,d}{2\,\hbar}\,\frac{\dddot{\tilde{k}}_x}{\omega_{\mathrm{C}}^2}. \tag{30}$$

Integration results in

$$x = \int v_x \, \mathrm{d}t + C = C - \frac{\Delta\,d}{2\,\hbar}\,\frac{\ddot{\tilde{k}}_x}{\omega_{\mathrm{C}}^2}. \tag{31}$$

With the initial conditions $x(0) = 0$ and $\tilde{k}_x(0) = \tilde{k}_{x,0} = 0$, we obtain with equation (7)

$$x = \frac{\Delta\,d}{2\,\hbar}\,\frac{1}{\omega_{\mathrm{C}}^2}\left(\omega_{\mathrm{B}} - \ddot{\tilde{k}}_x\right). \tag{32}$$

$\dot{\tilde{k}}_x$ can be substituted with the help of equations (19) and (17), which result in

$$\omega_B^2 = \dot{\tilde{k}}_x^2 + 4\,\omega_C^2 \, \sin^2(\tilde{k}_x/2), \tag{33}$$

yielding

$$\dot{\tilde{k}}_x = \pm \sqrt{\omega_B^2 - 4\,\omega_C^2 \, \sin^2(\tilde{k}_x/2)}. \tag{34}$$

We first consider the magneto-Bloch regime ($\omega_B > 2\omega_C$). In analogy to the rotating pendulum, which can rotate either left- or right-handedly, $\dot{\tilde{k}}_x$ does not change sign any more after the motion has started. The sign itself depends on the direction of the electric field **E** which determines the sign of the initial value of $\dot{\tilde{k}}_x$. With both q and E chosen to be positive, equation (17) yields $\dot{\tilde{k}}_x(0) = +|\omega_B|$, which fixes the sign in equation (34) to be positive. From equations (32) and (34), the displacement evaluates to

$$x = \frac{\Delta\,d}{2\,\hbar}\frac{\omega_B}{\omega_C^2}\left(1 - \sqrt{1 - 4\frac{\omega_C^2}{\omega_B^2}\,\sin^2(\tilde{k}_x/2)}\right). \tag{35}$$

The maximum displacement x_{max} is reached for $\tilde{k}_x = \pi$:

$$x_{max} = \frac{\Delta\,d}{2\,\hbar}\frac{\omega_B}{\omega_C^2}\left(1 - \sqrt{1 - 4\frac{\omega_C^2}{\omega_B^2}}\right). \tag{36}$$

For small magnetic fields, we approximate

$$\left(1 - \sqrt{1 - \left(2\frac{\omega_C}{\omega_B}\right)^2}\right) \approx 2\frac{\omega_C^2}{\omega_B^2}, \tag{37}$$

and obtain the following result for x_{max}:

$$x_{max} = \frac{\Delta\,d}{\hbar}\frac{1}{\omega_B} = 2L. \tag{38}$$

As expected, $x_{max}/2$ converges to the spatial amplitude L of pure BOs [33–35]. With increasing magnetic field (increasing ω_C), x_{max} increases steadily and reaches its maximum at the transition. There, $\omega_B = 2\omega_C$, resulting in

$$x_{max,\,MB} = \frac{\Delta\,d}{2\,\hbar}\frac{\omega_B}{\omega_C^2} = \frac{\Delta\,d}{2\,\hbar}\frac{4}{\omega_B} = 4L. \tag{39}$$

In the case of the cyclotron-like regime of motion ($\omega_B < 2\omega_C$), $\dot{\tilde{k}}_x$ changes sign time and again (oscillating pendulum) and equation (32) becomes maximal when $\dot{\tilde{k}}_x$ reaches its minimal value of $-\omega_B$ (equation (34)), so that

$$x_{max} = \frac{\Delta\,d}{\hbar}\frac{\omega_B}{\omega_C^2}. \tag{40}$$

With increasing magnetic field, x_{max} decreases towards zero. Its maximum is at B_T and amounts to

$$x_{max,\,cyclo} = \frac{\Delta\,d}{\hbar}\frac{4}{\omega_B} = 8L. \tag{41}$$

The dependence of x_{max} on the ratio ω_C/ω_B is shown in figure 10. The discontinuity at the transition between the two regimes can be explained by considering the pendulum for two slightly different total energies, one being just above, the other just below the critical (transition)
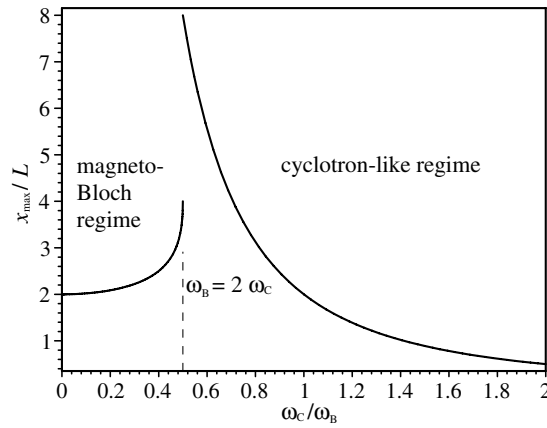
Figure 10. Maximum spatial wavepacket displacement (full swing) in units of the amplitude L of pure BOs versus the ratio ω_C/ω_B. Note the discontinuity at $\omega_C = \omega_B/2$, i.e., at the transition between magneto-Bloch and cyclotron-like regimes.

value. In the first case, the energy is sufficient for the pendulum to overcome the upper unstable fixed point, in the other case not. Let us consider the motion starting at an angle of $\varphi = 0$. When the pendulum moves towards the unstable fixed point at $\varphi = \pi$, it can pass it in the first case, but in the second case stops for a moment and reverses direction before reaching the fixed point. In both cases, $\varphi = 0$ is reached again after nearly the same time interval t' but with the pendulum moving in opposite directions. In the first case, one oscillation period is then over, while only half a period has elapsed in the second case.

Recalling that φ and $\tilde{k}_x$ correspond to each other, we can now consider the real-space velocity v_x of a charge carrier in the superlattice. Employing $v_x \propto \sin(\tilde{k}_x)$ (equation (5)), we find that v_x, in the magneto-Bloch regime, is positive during the first half of the time interval t' and negative during the second half. After t', the charge carrier is back at its starting point in real space. In the cyclotron-like regime, instead, v_x remains positive during the whole time range t' and only afterwards changes sign. This implies that the charge carrier reaches its maximum displacement from the starting point only at $t = t'$. If the total energies are similar in the two cases, the similar absolute values of the speed during the time interval explain that the maximal displacement is twice as large in the cyclotron-like regime.

3.2.2. Time-averaged spatial x-displacement. Considering now $\bar{x}$, the average spatial displacement in the x-direction, one finds that the values for the two regimes converge at the transition point. This can be illustrated nicely with the help of figure 11, which plots the time-dependent displacements $x(t)$ in the vicinity of the transition point. In both regimes of motion, the charge carriers spend much of the time at a distance close to $x_{\text{max, MB}} = 4L$, the maximum displacement of the magneto-Bloch regime. Only for a relatively short time—and with an ever lower frequency as the transition is approached, their motion over- or undershoots this x-value.

The average spatial displacement in the cyclotron-like regime of motion is only half the respective maximum value $x_{\text{max, cyclo}} = 8L$. In contrast, in the magneto-Bloch regime, the average displacement is somewhat smaller than $x_{\text{max, MB}}$, but increases towards this value as the transition is approached. The average displacements in both regimes hence converge at $x_{\text{max, MB}} = 4L$ at the transition, so that the average spatial displacement does not show a discontinuity here.
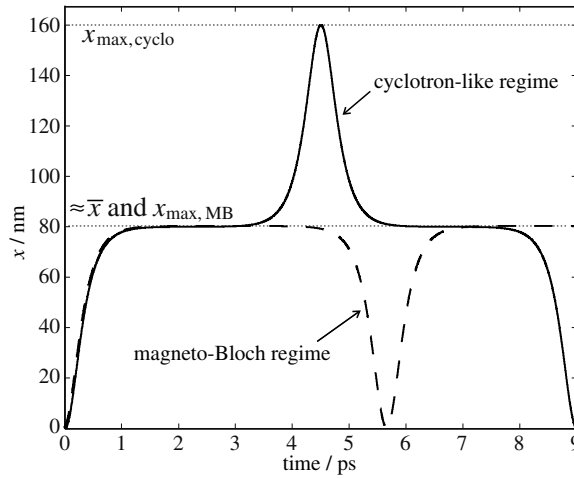
Figure 11. Time dependence of the spatial wavepacket displacement along the superlattice growth direction illustrating the difference between maximum and average displacement (x_{max} and $\bar{x}$, respectively) in the two regimes of motion.

3.3. THz-emission spectroscopy—expected transients and their frequency spectrum

The non-linear character of the wavepacket dynamics suggests that experimental signatures of the periodic wavepacket motion should exhibit a spectrum of frequencies and not only the fundamental frequency. In this section, we calculate the expected waveforms of THz transients emitted by the oscillating charge carriers and investigate their frequency spectrum.

In [19], we have presented time-domain THz-emission data where the radiation originates from the dipole moments associated with the motion of the charge carriers in the y-direction, i.e., perpendicular to the superlattice growth direction. Quantitatively, the electric field strength of the detected radiation $E_{THz,y}$ is proportional to the second time derivative of the corresponding component of the polarization P_y [36, 37]:

$$E_{THz,y} \propto \frac{d^2 P_y}{dt^2} \propto q\, \dot{v}_y. \tag{42}$$

Figure 12 displays numerically calculated data of $E_{THz,y}$ for a constant electric bias field of $5\ \text{kV cm}^{-1}$ and for magnetic fields between 0.1 and 3.5 T. In order to be close to experimental reality, dephasing with a time constant of 1 ps is assumed. One can clearly distinguish the manifestations of the two regimes of motion with their different magnetic-field dependences of the fundamental frequency. In addition, one identifies the transition region where the amplitude of the oscillations decreases and higher harmonic frequencies contribute to the signal. Directly at the transition, the oscillations vanish (not displayed in the figure). We remark that, except for the direct vicinity of the transition region, the higher harmonics may be difficult to identify in measurements when these exhibit some measure of noise.

Figure 13 shows the frequency spectra of numerically calculated THz transients, now for a constant magnetic field of 1 T and electric fields between 2.5 and $4\ \text{kV cm}^{-1}$ varied in small steps of $10^{-4}\ \text{kV cm}^{-1}$. For the sake of clarity with respect to the higher harmonics, damping is omitted here. The grey scales are a measure for the amplitude: darker regions correspond to higher amplitudes in the frequency spectra. The time interval used for the Fourier analysis amounts to 50 ps, resulting in a frequency resolution of 20 GHz, which gives rise to the step-like shape of the curves. Besides the opposite frequency dependence in the two regimes, the
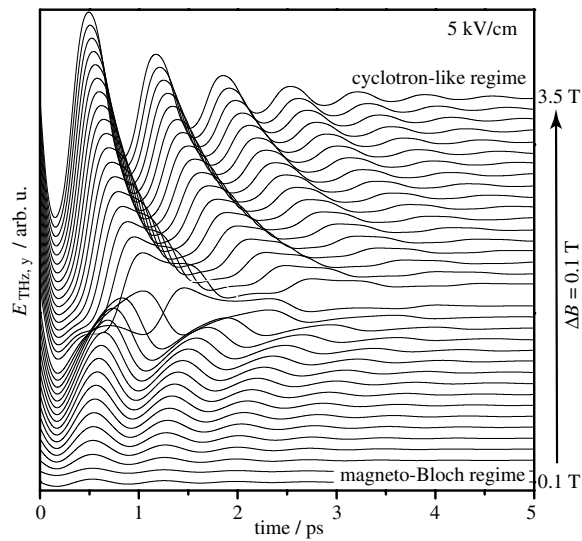
Figure 12. THz transients calculated for a constant electric bias field of 5 kV cm^{-1} and magnetic fields between 0.1 and 3.5 T (step width: 0.1 T). Dephasing with a time constant of 1 ps is assumed.
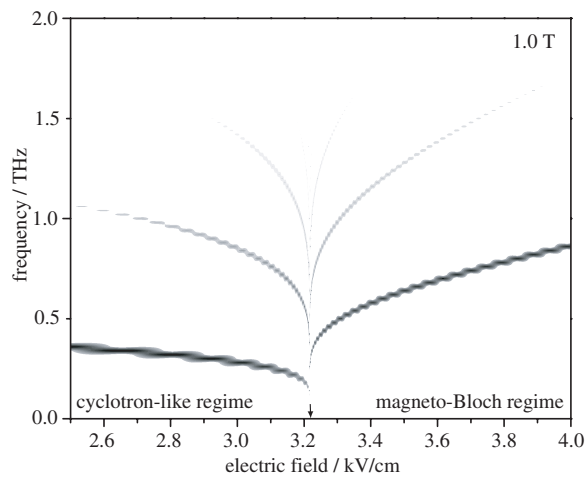

Figure 13. Frequency spectra of numerically calculated THz transients for a constant magnetic field of 1 T and electric fields between 2.5 and 4 kV cm^{-1} varied in steps of 10^{-4} kV cm^{-1}. The amplitude is indicated by grey scales with dark regions corresponding to high amplitudes. The step-like shape is caused by the time window of the Fourier analysis of 50 ps, resulting in a frequency resolution of 20 GHz. The arrow marks the transition point.

plot shows the sudden decrease of the frequencies and the simultaneous decrease of the overall signal amplitude towards the transition.

As mentioned above, higher harmonic frequencies become more important in this region. While only odd harmonics contribute in the cyclotron-like regime of motion, the frequency spectra in the magneto-Bloch regime close to the transition contain even and odd harmonics.
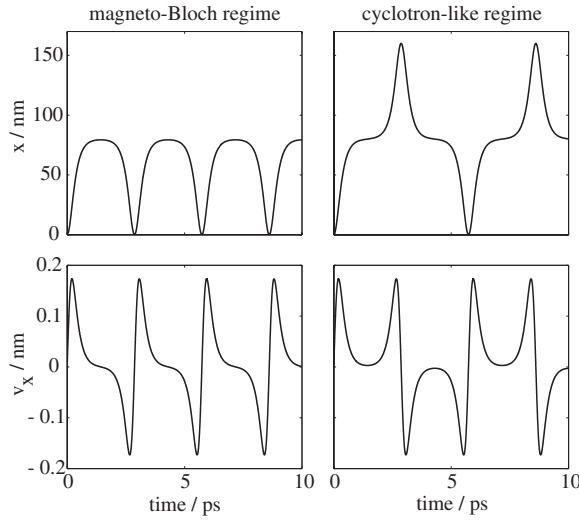
Figure 14. Time dependence both of the spatial displacement of the wavepacket (upper part) and of the velocity along the superlattice growth direction (lower part) calculated for a constant electric field of 5 kV cm^{-1} and a magnetic field which is smaller by $\Delta B = 5 \times 10^{-5}$ T than the magnetic field $B_T = 1.554\,4819\ldots$ T at the transition (magneto-Bloch regime, left side), respectively by the same amount larger than B_T (cyclotron-like regime, right side).

This can be understood in the following way. From equations (5), (6) and (42) one obtains

$$\dot{v}_y = \frac{\hbar}{m^*}\,\dot{k}_y = \frac{\hbar}{m^*}\,\left(-\frac{q}{\hbar}Bv_x\right) = -\omega_C^*\,v_x, \tag{43}$$

and therefore the relation

$$E_{\text{THz},y} \propto -\omega_C^*\,v_x. \tag{44}$$

The electric field strength of the emitted THz radiation is hence proportional to the wavepacket velocity $v_x = \dot{x}$ in the x-direction.

The time dependence of this quantity is shown in the lower part of figure 14 for both the magneto-Bloch and the cyclotron-like regimes of motion. The upper part of the figure displays the spatial x-displacement (compare figure 11). The figure illustrates that the function $v_x(t)$, when shifted by half its period, results in $-v_x(t)$ in the cyclotron regime, hence it is sufficient to employ odd harmonics in the Fourier analysis of $v_x(t)$. In contrast, such a symmetry does not exist in the magneto-Bloch regime, and one needs even and odd Fourier components to reproduce $v_x(t)$.

3.4. Internal electro-optic sampling—expected frequency spectrum

Another experimental technique which we have applied for the investigation of the coherent Hall effect is time-resolved internal electro-optic sampling either in transmission (TEOS) or in reflection (REOS) [21]. It probes essentially the polarization P_x associated with the wavepacket oscillations in the x-direction [13, 38, 39]:

$$\text{EO-signal} \propto P_x \propto q\,x. \tag{45}$$

Figure 15 shows calculated TEOS transients for a fixed electric field (5 kV cm^{-1}) and a series of magnetic fields (from 0.1 to 3.5 T in steps of 0.1 T). Damping with a time constant of 1.2 ps
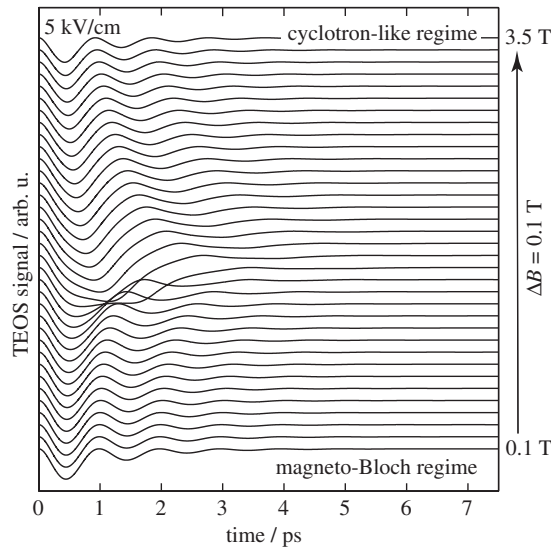
Figure 15. TEOS transients calculated for a constant electric bias field of 5 kV cm^{-1} and magnetic fields between 0.1 and 3.5 T (0.1 T steps). Dephasing with a time constant of 1.2 ps is assumed.

is assumed. The transients exhibit again the characteristic signatures of the two regimes of carrier motion. Close to the transition, one identifies anharmonic signal components but they appear to be less pronounced than in the THz-emission transients (see figure 12).

Figure 16 compares the Fourier spectra of calculated TEOS signals with those of calculated THz-emission waves. The spectra exhibit a major difference in that the TEOS signal remains strong at the transition while the THz-emission data taper off in this range. The strongest TEOS signal is in fact observed in the cyclotron-like regime very close to the transition, because both the spatial wavepacket displacement and its time derivative are large here. The THz-emission signal, originating from carrier motion parallel to the quantum-well planes (*y*-direction), on the other hand, becomes weak, because all wavepacket oscillations disappear at the transition and only the initial carrier acceleration contributes to the signal.

The weakening of the THz-emission signal towards low magnetic fields is related to the fact that the magnetic field becomes less effective in bending the real-space trajectories of the carriers away from the *x*-direction and into the *y*-direction. Quite in contrast, the THz-emission signal is strong (while the TEOS signal becomes weak) for very high magnetic fields just because of the strong trajectory bending.

Interestingly, the relative contribution of higher harmonics is larger in the THz radiation than in the TEOS signal. To some degree, this is a consequence of the different orientations of the relevant polarization components. More important, however, is the fact that THz emission depends on the second time derivative of the polarization, while TEOS is determined by the polarization itself. In order to illustrate this, let us consider a polarization given by a Fourier series $P(t) = \sum_n A_n \exp(in\omega t)$. The TEOS signal then reproduces the contribution at the fundamental frequency ω and the higher harmonics with relative weights as given by the coefficients A_n. The THz radiation, on the other hand, reproduces each frequency component with a weight of $n^2\omega^2 A_n$. Because n^2 enters the weight factor, higher harmonics are more pronounced.
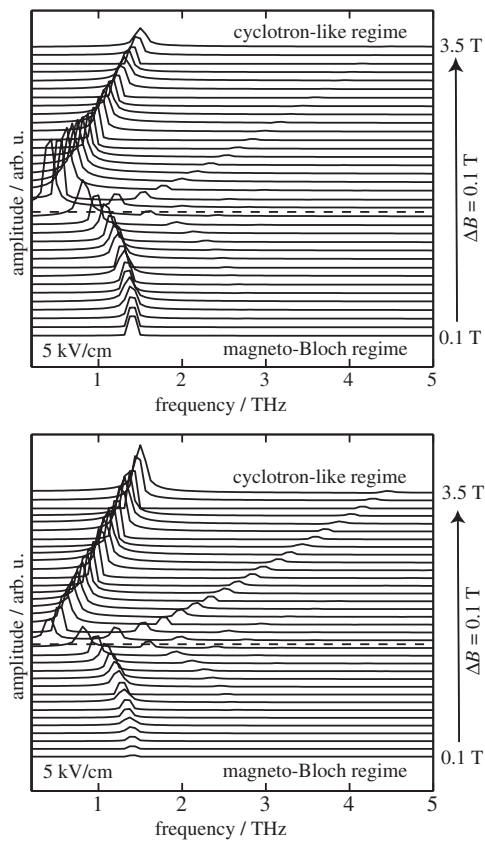
Figure 16. Comparison of the Fourier amplitude spectra of a calculated TEOS signal (upper part) and a THz-emission wave (lower part). The calculations assume a constant electric field of 5 kV cm^{-1}; the strength of the magnetic field is varied from 0.1 to 3.5 T in steps of 0.1 T. Dephasing is neglected for clarity; the line width of the spectral features is determined by the time window of 16 ps of the calculations.

4. Summary

In conclusion, we have investigated the electron wavepacket motion in a superlattice subjected simultaneously to an electric field in the growth direction and to a perpendicular magnetic field. The coherent electron dynamics has been studied for low carrier density by a numerical evaluation of the semiclassical, scattering-free, single-particle equation of motion. As it is analogous to the pendulum's equation of motion, one obtains two regimes of motion. The focus of our study has been on the transition between these two regimes, which are characterized by magneto-Bloch oscillations respectively cyclotron-like oscillations of the carriers. The oscillation frequency collapses to zero at the transition and the spatial displacement of the carriers upon crossing of the transition is discontinuous, reaching a maximum value of eight times the Bloch-oscillation amplitude when the transition point is approached from the cyclotron-like regime. We have shown that the electrons gain substantial kinetic energy much larger than the miniband width in the vicinity of the transition. In addition, the motion is highly anharmonic there with the wavepacket oscillations containing higher harmonics. Only odd harmonics appear in the cyclotron-like regime, while even and odd harmonics contribute in the

magneto-Bloch regime. Finally, a simulation of both THz-emission and internal-electro-optic-sampling spectroscopy predicts the former to be better suited for an experimental study of the higher harmonics.

Acknowledgments

References

[1] Bloch F 1928 *Z. Phys.* **52** 555
[2] Zener C 1934 *Proc. R. Soc.* A **145** 523
[3] Esaki L and Tsu R 1970 *IBM J. Res. Dev.* **14** 61
[4] Leo K 2003 *High-Field Transport in Semiconductor Superlattices* (Berlin: Springer)
[5] Feldmann J, Leo K, Shah J, Miller D A B, Cunningham J E, Meier T, von Plessen G, Schulze A, Thomas P and Schmitt-Rink S 1992 *Phys. Rev.* B **46** R7252
[6] Leo K, Haring-Bolivar P, Brüggemann F, Schwedler R and Köhler K 1992 *Solid State Commun.* **84** 943
[7] Waschke C, Roskos H G, Schwedler R, Leo K, Kurz H and Köhler K 1993 *Phys. Rev. Lett.* **70** 3319
[8] Feldmann J 1992 Festkörperprobleme *Adv. Solid State Phys.* **32** 81
  Leo K 1992 Festkörperprobleme *Adv. Solid State Phys.* **32** 97
  Roskos H G 1995 Festkörperprobleme *Adv. Solid State Phys.* **34** 297
[9] Dekorsy T, Leisching P, Köhler K and Kurz H 1994 *Phys. Rev.* B **50** R8106
  Leisching P, Haring-Bolivar P, Beck W, Dhaibi Y, Brüggemann F, Schwedler R, Kurz H, Leo K and Köhler K 1994 *Phys. Rev.* B **50** 14389
  Leisching P, Beck W, Kurz H, Schäfer W, Leo K and Köhler K 1995 *Phys. Rev.* B **51** R7962
[10] Waschke C, Leisching P, Haring-Bolivar P, Schwedler R, Brüggemann F, Roskos H G, Leo K, Kurz H and Köhler K 1994 *Solid State Electron.* **37** 1321
[11] Waschke C, Roskos H G, Leo K, Kurz H and Köhler K 1994 *Semicond. Sci. Technol.* **9** 416
  Dekorsy T, Leisching P, Waschke C, Köhler K, Leo K, Roskos H and Kurz H 1994 *Semicond. Sci. Technol.* **9** 1959
[12] Roskos H G, Waschke C, Schwedler R, Leisching P, Dhaibi Y, Kurz H and Köhler K 1994 *Superlatt. Microstruct.* **15** 281
  Dekorsy T, Leisching P, Beck W, Ott R, Dhaibi Y, Kurz H and Köhler K 1994 *Superlatt. Microstruct.* **15** 11
[13] Dekorsy T, Ott R, Kurz H and Köhler K 1995 *Phys. Rev.* B **51** R17275
[14] Kurz H, Roskos H G, Dekorsy T and Köhler K 1996 *Phil. Trans. R. Soc.* A **354** 2295
[15] von Klitzing K, Dorda G and Pepper M 1980 *Phys. Rev. Lett.* **45** 494
[16] Tsui D C, Störmer H L and Gossard A C 1982 *Phys. Rev. Lett.* **48** 1559
[17] Kosevich Y A 1999 *Ann. Phys.* **8** SI-145
[18] Kosevich Y A 2001 *Phys. Rev.* B **63** 205313
[19] Bauer T, Kolb J, Hummel A B, Roskos H G, Kosevich Y and Köhler K 2002 *Phys. Rev. Lett.* **88** 086801
[20] Bauer T 2002 Kohärenter Hall-Effekt in einem Halbleiter-Übergitter *PhD Thesis* Department of Physics, University of Frankfurt
[21] Hummel A B, Blöser C, Bauer T, Roskos H G, Kosevich Y A and Köhler K 2005 *Phys. Status Solidi* b **242** 1175
[22] Fromhold T M, Krokhin A A, Tench C R, Bujkiewicz S, Wilkinson P B, Sheard F W and Eaves L 2001 *Phys. Rev. Lett.* **87** 046803
[23] Fromhold T M, Patanè A, Bujkiewicz S, Wilkinson P B, Fowler D, Sherwood D, Stapleton S P, Krokhin A A, Eaves L, Henini M, Sankeshwar N S and Sheard F W 2004 *Nature* **428** 726
[24] Stapleton S P, Bujkiewicz S, Fromhold T M, Wilkinson P B, Patanè A, Eaves L, Krokhin A A, Henini M, Sankeshwar N S and Sheard F W 2004 *Physica* D **199** 166
[25] Kosevich Y A 2003 *Phys. Status Solidi* c **0** 1467
[26] Kosevich Y A, Hummel A B, Roskos H G and Köhler K 2006 *Phys. Rev. Lett.* at press
[27] Löser F, Kosevich Y A, Köhler K and Leo K 2000 *Phys. Rev.* B **61** R13373

[28] Kosevich Y A 2002 *Phys. Rev. Lett.* **88** 229701

[29] Haug H and Koch S W 1993 *Quantum Theory of the Optical and Electronic Properties of Semiconductors* 2nd edn (Singapore: World Scientific)

[30] Grahn H T 1995 *Semiconductor Superlattices* (Singapore: World Scientific)

[31] von Plessen G, Meier T, Feldmann J, Göbel E O, Thomas P, Goossen K W, Kuo J M and Kopf R F 1994 *Phys. Rev.* B **49** R14058

[32] Hader J, Meier T, Koch S W, Rossi F and Linder N 1997 *Phys. Rev.* B **55** 13799

[33] Martini R, Klose G, Roskos H G, Kurz H, Grahn H T and Hey R 1996 *Phys. Rev.* B **54** R14325

[34] Lyssenko V G, Valusis G, Löser F, Hasche T, Leo K, Dignam M M and Köhler K 1997 *Phys. Rev. Lett.* **79** 301

[35] Leo K 1998 *Semicond. Sci. Technol.* **13** 249

[36] Roskos H G, Nuss M C, Shah J, Leo K, Miller D A B, Fox A M, Schmitt-Rink S and Köhler K 1992 *Phys. Rev. Lett.* **68** 2216

[37] Meier T, von Plessen G, Thomas P and Koch S W 1994 *Phys. Rev. Lett.* **73** 902

[38] Kütt W A, Albrecht W and Kurz H 1992 *IEEE J. Quantum Electron.* **28** 2434

[39] Lövenich R, Victor K, Bartels G, Stahl A, Müller A, Haring-Bolivar P, Dekorsy T and Kurz H 1997 *Solid State Commun.* **101** 167